# Design and Construction of Field Reversed Configuration Plasma Chamber for Plasma Material Interaction Studies

**DuWayne L. Smith**

A Thesis
submitted in partial fulfilment of the
requirements for the degree of
Master of Material Science and Engineering

University of Washington

2014

Committee:

Fumio S. Ohuchi
John T. Slough
George R. Votroubek
Peter J. Pauzauskie

Program Authorized to Offer Degree:
Materials Science and Engineering

University of Washington

## Abstract

Design and Construction of Field Reversed Configuration Plasma Chamber for Plasma Material Interaction Studies

DuWayne L. Smith

Chair of the Supervisory Committee:
Professor & Associate Chair Dr. Fumio S. Ohuchi
Materials Science and Engineering

*A Field Reversed Configuration (FRC) plasma source was designed and constructed to conduct high energy plasma-materials interaction studies. The purpose of these studies is the development of advanced materials for use in plasma based electric propulsion systems and nuclear fusion containment vessels. Outlined within this thesis is the basic concept of FRC plasmoid creation, an overview of the device design and integration of various diagnostics systems for plasma conditions and characterization, discussion on the variety of material defects resulting from the plasma exposure with methods and tools designed for characterization. Using a Michelson interferometer it was determined that the FRC plasma densities are on the order of* $\sim 10^{21}\ m^{-3}$*. A novel dynamic pressure probe was created to measure ion velocities averaging 300 km/s. Compensating flux loop arrays were used to measure magnetic field strength and verify the existence of the FRC plasmoid and when used in combination with density measurements it was determined that the average ion temperatures are ~130 eV. X-ray Photoelectron Spectroscopy (XPS) was employed as a means of characterizing the size and shape of the plasma jet in the sample exposure positions. SEM results from preliminary studies reveal significant morphological changes on plasma facing material surfaces, and use of XRD to elucidate fuel gas-ion implantation strain rates correlated to plasma exposure energies.*

# Table of Contents

# 1. Introduction

## 1.1 Plasma Material Interactions

Over the past 20 years the study of plasma-materials interactions have been validated through countless modern processing techniques that utilize the high energy, dimensionality and chemical reactivity of plasmas to create some of the most technically advanced tools in existence today. From plasma etching of microchips to the promise of fusion based pulsed power systems, plasma science will continue to evolve as a fundamental and highly specialized field with broad ranging applications. Because of the complexity of plasma-materials interactions, which often encompass the interaction of matter in four different states, it is of great importance that a reliable test bed be used to conduct such studies [1]. The ability to accurately and efficiently characterize plasma dynamics and energies in relation to physical and chemical mutations of solids resulting directly from ion exposures is crucial to the development of plasma devices and processing techniques.

The current paradigm suggests that all matter in the universe exists in one of four states. This state is dependent on its relative intrinsic energy which can be classified by its temperature. These states include: solids, liquids, gases and plasmas; the solid form being the lowest energy state, and plasma being the highest. It is estimated that 99% of all visible matter in the universe is in the form of plasma and interactions between plasmas and solid state materials have proven to be extremely useful in a variety of technical designs and processes. It is therefore critical that we understand this dynamic and the unique chemical and physical phenomena that result from the extreme difference in energies. Formally, plasma is characterized as an electrically neutral system of ionized particles wherein the particles themselves have kinetic energies greater than the ionization energies of the fuel gas. This situation creates a system of unbound electrons and ionized particles acting much like a charged fluid with random kinetic energies that far exceed the average electrostatic energies thus making long range forces dominant over any short range forces [2]. The system is therefore controlled primarily by its own electric and magnetic fields that dictate its shape, density and flow giving rise to the term magneto hydrodynamic fluid or MHD.

Recent investigations into the chemical and physical dynamics of plasma produced inside reactor cores have revealed a significant problem with the stability of materials used in plasma facing positions. Materials exposed to transient non-equilibrium, chemically reactive, highly magnetized plasmas experience a high rate of erosion resulting in a number of undesirable effects. When plasma impinges onto the surface of a solid state material a variety of chemical and physical phenomena occur. The most dramatic of which is the cascade of collisions that occurs between atoms on the surface when hit directly by fast ions, and in fusion grade plasmas, neutrons. A standard characterization for materials in this context uses the term DPA, which is

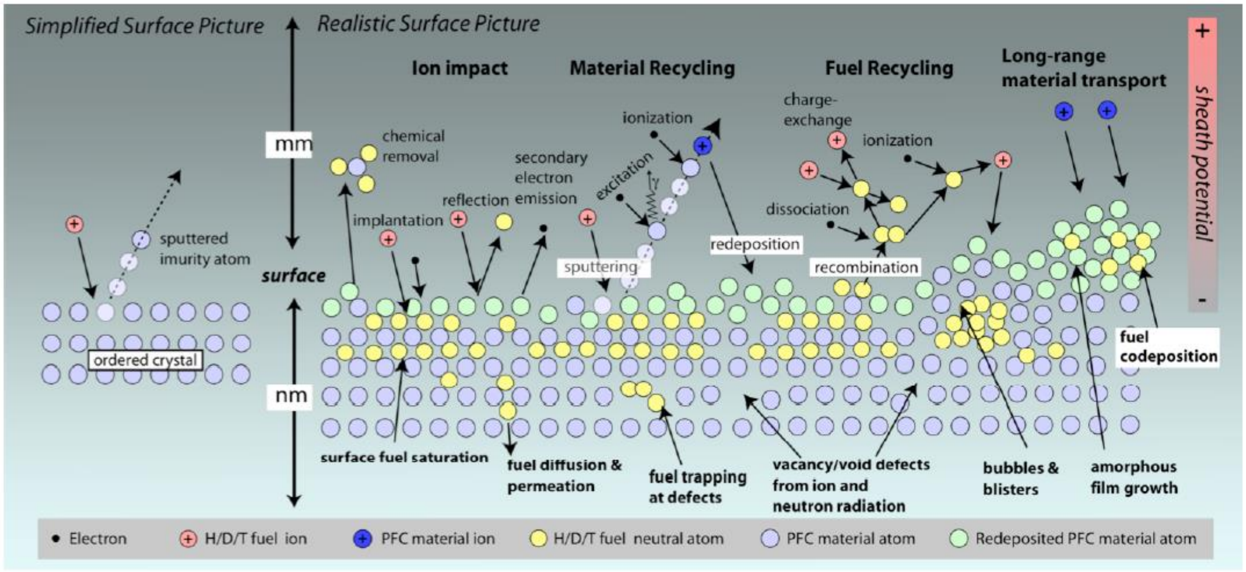

**Figure 1.1: Atomic scale model of material surface being exposed to highly energetic plasma. The various physical and chemical dynamics can be seen to occur simultaneously on the material surface and clearly illustrate the complex nature of the interaction and resulting damage.**

an acronym for dislocations per atom and can directly describe the extent or volume of the affected area. As can be seen in figure 1.1, this interaction dramatically alters the chemistry and physical morphology of the surface and typically destroys the local crystal structure resulting in an amorphous region void of any previous mechanical, electrical or optical properties. This region becomes highly concentrated with lattice point vacancies which can agglomerate creating large voids. In the case of ionic crystals, Frenkle pairs are formed and chemical segregation on the surface often occurs. Furthermore, physical sputtering of surface material results in uncontrolled re-deposition and plasma contamination. Plasma fuel gas retention is also a problem which can result in stress related corrosion and undesirable desorption rates which can intern denature plasma conditions. In the case of high density plasmas, such as those found in fusion grade plasmas, neutron and photon radiation can significantly damage the plasma facing surfaces in a number of thermal, chemical and physical modes.

Currently there is a great deal of focus on using plasma as a propellant for space craft as well as in the design of pulsed power nuclear fusion for large scale energy generation. In this context the aforementioned issues of material damage become significant to the long range performance of plasma based devices. In fact, the material science component in their development becomes crucial to the operational longevity of these very expensive and complicated devices. It is important that materials used in plasma facing positions be developed in tandem with increasing plasma densities and energies. A program at the University of Washington that combines the expertise of plasma physics and materials science researchers has been developed that seeks to advance the field of high temperature materials, space propulsion and electro-energetic physics research. With the discovery of a new class of electromagnetic pulsed plasma propulsion devices such as the Electrodeless Lorentz Force (ELF) Thruster [3], it is critical to characterize and develop new materials for these systems that can withstand the demanding conditions of space propulsion or directed energy.

## 1.2 Plasma Source and Characterization

In order to generate measurable chemical and physical changes in the material samples plasma energies should range between 1kJ/m$^2$ and 1MJ/m$^2$. In these experiments a relatively new approach to generating hot dense plasmas was employed. Classified as a Field Reversed Configuration (FRC) plasma source, this technique utilizes a fast reversal of magnetic field direction to create a closed magnetic field profile that effectively traps and compresses an ionized gas into a compact toroid structure known as a "plasmoid". The plasmoid has a lifetime governed by the L/R decay of a current ring and as it decays it ejects hot dense plasma in jets that propagate axially from each side. FRC's are well studied [4,5] and commonly yield plasma densities on the order of ~10$^{21}$ m$^{-3}$ and can be translated with ion velocities ~10$^5$ m/s. It is within the axial jet that the material samples will be positioned. FRC's are typically created in a low pressure environment where fuel gas pressures can be controlled and contaminants are in low concentrations. This requires magnetic coils in a solenoid type configuration to be placed around an evacuated tube such that an ionized gas can be positioned within the tube and coils. Current is driven through the coils in a manner that creates a series of very specific magnetic field profiles that generate the plasmoid. The ends of the coil must have a larger current density to reduce field divergence and "pinch" the plasma as it is being compressed. There are five primary steps to creating a plasmoid as illustrated in figure 1.2. The first is the application of a relatively strong negative magnetic bias within the formation chamber. This provides the flux that will be trapped in the plasma and converted to a rotational ion current once the plasmoid is formed. The field is then quickly and intensely switched to a positive bias. This rapid reversal of field polarity and

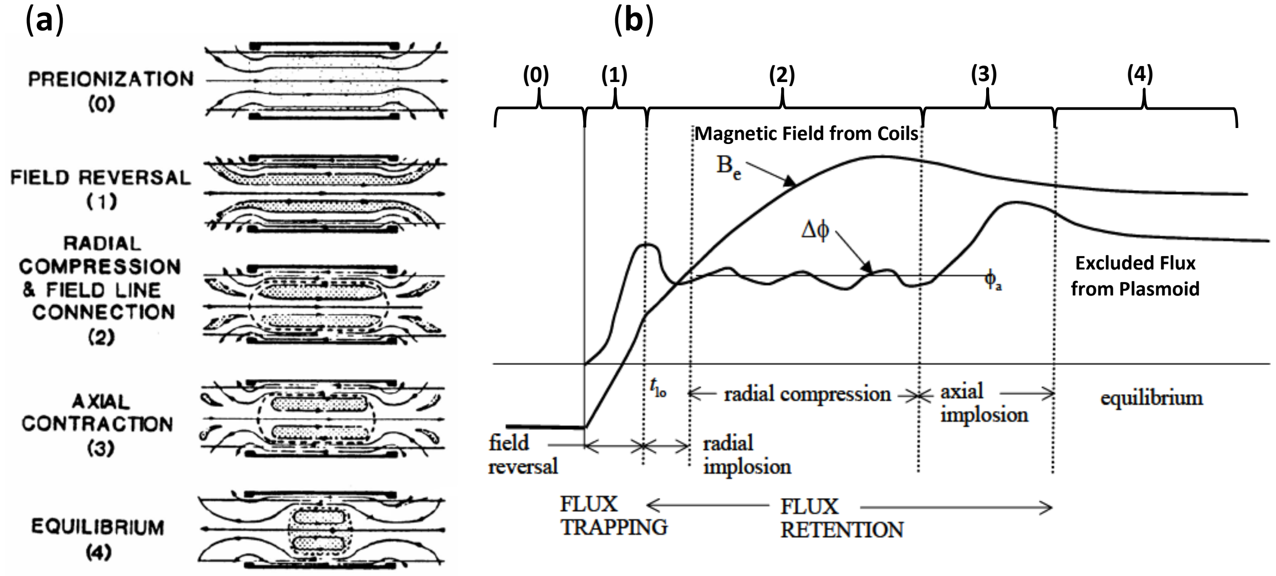

**Figure 1.2: (a) Step-by-step illustration for plasmoid formation and (b) characteristic waveforms for both external magnetic field profile necessary for creation of the plasmoid and the excluded flux resulting from the diamagnetic response of the toroidal currents. Class notes courtesy of Professor A. L. Hoffman (2006), University of Washington Aero-astro department[4].**

increased field strength on the end coils effectively trap magnetic flux resulting in a closed field loop seperatrix. The ions therefore become trapped and begin to rotate around the central axis resulting in a radial compression. As the external field increases the ends of the toroidal shaped MHD are pushed inward increasing the ion rotation and density until the plasma pressure is equal to the external field strength and the plasmoid is formed. The toroidal currents in the plasmoid give the object a diamagnetic response to the external field, in turn the plasmoid acts as a flux excluder pushing field away as it reaches equilibrium. The excluded flux can be measured to verify the existence of the plasmoid and calculate its size. Figure 1.3 is a diagram illustrating the shape of the plasmoid and parameters needed to determine its diameter. Here $B_e$ is the external field that corresponds to the exterior flux produced from the diamagnetic response during the existence of the plasmoid, $B_0$ is the vacuum field from the coils. The ratio of $B_e$ to $B_0$ is [5]:

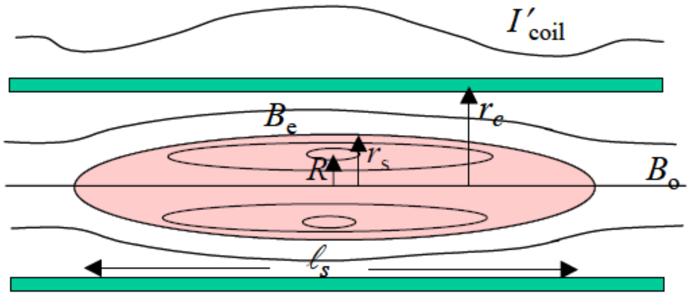

**Figure 1.3: Illustration elongated toroidal shaped cross section of plasmoid with external field and radial variables [4].**

$$\boldsymbol{\frac{B_o}{B_e} = 1 - \left(\frac{r_s}{r_c}\right)^2} \qquad \text{eq. } \mathit{1.2.1}$$

Where $r_c$ is the coil radius, R is the torus major radius and $r_s$ is the minor radius or plasmoid radius. Both the excluded flux and external flux from the coils can be measured using a compensating flux loop array positioned on the exterior and interior diameter of each coil.

In order to conduct such studies it is important to be able to accurately diagnose plasma conditions at the point of contact with the material sample. There are several important plasma parameters that need be known in order to characterize damage in a material related to plasma conditions. Parameters which are most important include; ion velocities, temperature and energy fluence. Energy fluence is of specific interests as it describes the energy experienced by the material surface per pulse and can be calculated from the following relation:

$$\boldsymbol{\Phi_E = \frac{1}{2} n t m_i v^3} \qquad \text{eq. } \mathit{1.2.2}$$

Here, $m_i$ is the mass of the ion, $v$ is the ion velocity $n$ is the particle density and $t$ is the duration of the plasma pulse. It can be seen that the fluence is highly dependent on the velocity of the ion. Densities can be measured with a standard Michelson Interferometer. With the particle density and external poloidal field known it is possible to calculate the plasma temperature from the expression [5]:

$$\boldsymbol{\beta = \frac{nkT}{B_e^2/2\mu_o}} \qquad \text{eq. } \mathit{1.2.3}$$

In this relation $\beta$ is the radial pressure balance, $k$ is Boltzmann's constant, $T$ is the temperature of the electrons and $\mu_o$ is the permeability of free space. During the existence of the plasmoid the radial pressure balance is assumed to be unity. Plasmas in thermodynamic equilibrium where the electrons are at essentially the same temperature as the ions, the velocity and temperature are related by the following expression [3]:

$$\langle \frac{1}{2} \boldsymbol{m_i v^2} \rangle = \frac{3}{2} \boldsymbol{kT_i} \qquad \text{eq. } \mathit{1.2.4}$$

Here $T_i$ is the temperature of the ion. However, in the case where the external electric and magnetic fields are sufficiently strong, such as those created in FRC's which produce very dense and energetic plasmas, the non-equilibrium situation arises where the temperature of the ions and electrons are not equal, it becomes necessary to measure plasma temperature and velocities independently.

## 1.3 Material Exposure and Characterization

Material exposures are the focus of the study and the plasma source must be designed to facilitate the interaction. The samples will be placed within the plasma jet created by the plasmoid as it decays; therefore the sample exposure positions need to be as close to the central axis of the plasmoid to be hit by the most energetic portion of the jet. Figure 1.4 is a schematic that shows the intended positions of the material sample relative to the plasma jet. The jet is contained by the cusp coils which extend axially from both sides of the plasmoid formation section. These coils can be controlled to vary the magnetic field strength and subsequently the plasma jet radius and density. The sample can also be positioned at different distances from the end of the plasmoid for further variation of the plasma exposure. The sample cannot be placed inside the plasmoid or pinch coil section as that would disturb the magnetic field profile and the plasmoid would not be able to be formed.

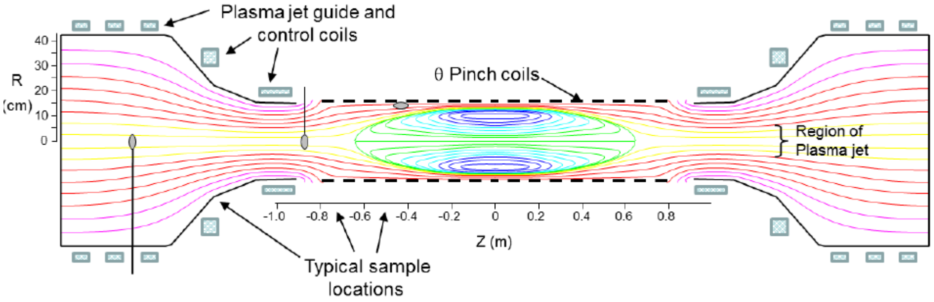

**Figure 1.4: Schematic illustrating the sample positions within the plasma jet. Yellow magnetic field lines indicate the most energetic ion pathways. Green and purple indicate the plasmoid.**

After the materials have been exposed to a specified number of pulses or “shots” it can be analyzed in a variety of ways. Optical Microscopy can be used to observe macroscopic damage to the surface as well as discoloration resulting from chemical changes or variance in redeposition thickness. Scanning Electron Microscopy (SEM) can be used to observe morphological changes to the surface in great detail at the nano-meter scale, in conjunction with Energy Dispersive X-rays (EDX) to observe the existence of specific elements.

X-ray Photoelectron Spectroscopy (XPS) is a powerful tool that can be used to identify finer chemical details on the sample surface resulting from the exposure which includes chemical bonding information. XPS can also be used with a low energy argon sputtering technique to perform a depth profile study of chemical interactions resulting from the penetration of plasma fuel gas ions or impacts with pre-existing surface elements. The results can be used to identify ion penetration depths which is an important parameter used for material selection.

Defects such as vacancies and dislocations are typically characterized through TEM. However, this method is known to be particularly difficult because it requires careful preparation of the sample. It is possible to characterize these types of defects with Raman Spectroscopy [5]. Because each type of defect, particularly vacancies, will have a localized effect on the vibrational mode of its environment, it is possible to measure the intensity of these signature vibrational modes to gain information about the change in vacancy and dislocation densities related to the plasma exposure.

Fuel gas retention and desorption is another factor that plays an important role in material selection and is therefore an important focus in plasma material interaction studies. Thermal Desorption Spectroscopy (TDS) can be used to measure not only the amount of fuel gas retention within the material, but also the rate at which it is desorbed as the material heats up during device operation. From this technique desorption rates and desorption activation energies can be characterized for any group of materials.

One of the most important aspects of material selection is in the materials ability to withstand stress from both ion and neutron implantation as well as thermal radiation. Stress induced by ion and neutron implantation can be found by the change in lattice parameters of the materials specific unit cell and therefor can be measured using X-ray Diffraction Spectroscopy (XRD). From Bragg's law the change in *d* spacing can be found and the strain (*Δd/d)* on the material can be derived:

$$\frac{\Delta d}{d_i} = \frac{\lambda_{K\alpha}}{2d_i}\left(\frac{1}{sin\theta_f} - \frac{1}{sin\theta_i}\right) = \frac{sin\theta_i}{sin\theta_f} - 1 \qquad \text{eq.}1.3.1$$

Where $\theta_i$ is the initial theta value for the center of the peak representing the spacing between the two atomic planes in question, and $\theta_f$ is the final theta position measured from the exposed sample. With the strain known, the average stress ($\sigma$) in the material can be found from the relation:

$$\sigma_e = E\left(\frac{sin\theta_i}{sin\theta_f} - 1\right) \qquad \text{eq. } 1.3.2$$

Here, *E* is Young's Modulus. When the stress from the exposure exceeds the yield stress of the material it will begin to deform, and when it reaches the tensile stress cracking and flaking will occur which clearly defines the exposure limit. Therefore, it could be concluded that a reasonable figure of merit for stress related properties ($S_{FM}$) would include the following relation:

$$S_{FM} = \frac{\sigma_e/\sigma_y}{\mathrm{n}\cdot\Phi_E} \qquad \text{eq. } 1.3.3$$

Where ($\boldsymbol{\sigma_e/\sigma_y}$) is the ratio of stress from the plasma exposure to the yield stress and ($\mathbf{n}\cdot\boldsymbol{\Phi_E}$) is the total energy experienced by the sample from multiple shots.

In summary the focus of this research assignment was the development of a reliable method to study plasma material interactions in high energy regimes. The objective was to induce significant physical and chemical changes in materials with characteristic properties suitable for plasma facing surfaces. Materials with intrinsic properties most suitable for these extreme environments such as strength, thermal conductivity and chemical stability were selected for study. The project ultimately involved the development of an FRC plasma source with integrated plasma diagnostic systems and sample exposure stage. The post exposure material analysis involved primarily sputter – redeposition studies, physical and chemical transitions, ion implantation and lattice expansion with the primary analytical tools being optical microscopy, SEM, XPS and XRD. The following sections outline the specific details of the exposure chamber design, FRC plasmoid production, plasma characterization and resulting material analysis.

## 2. Design of the Plasma Source

### 2.1 Chassis and Vacuum System

The FRC chamber, where the plasmoid is formed, is a 10 cm ID, 60 cm long, quartz tube purchased from Hayward Quartz Technology Inc, and is centered between two ISO 100/NW 50 stainless steel four way crosses that support the experiment and provide ports for pumping and plasma diagnostics. The formation chamber is pumped out on both using two mini Boc Edward turbo pumps that maintain a base pressure in the mid $10^{-7}$ Torr and are electrically isolated from the formation chamber by quartz nipples. The background pressures are monitored with standard thermocouple and cold cathode gauges and contamination profiles with partial pressures are

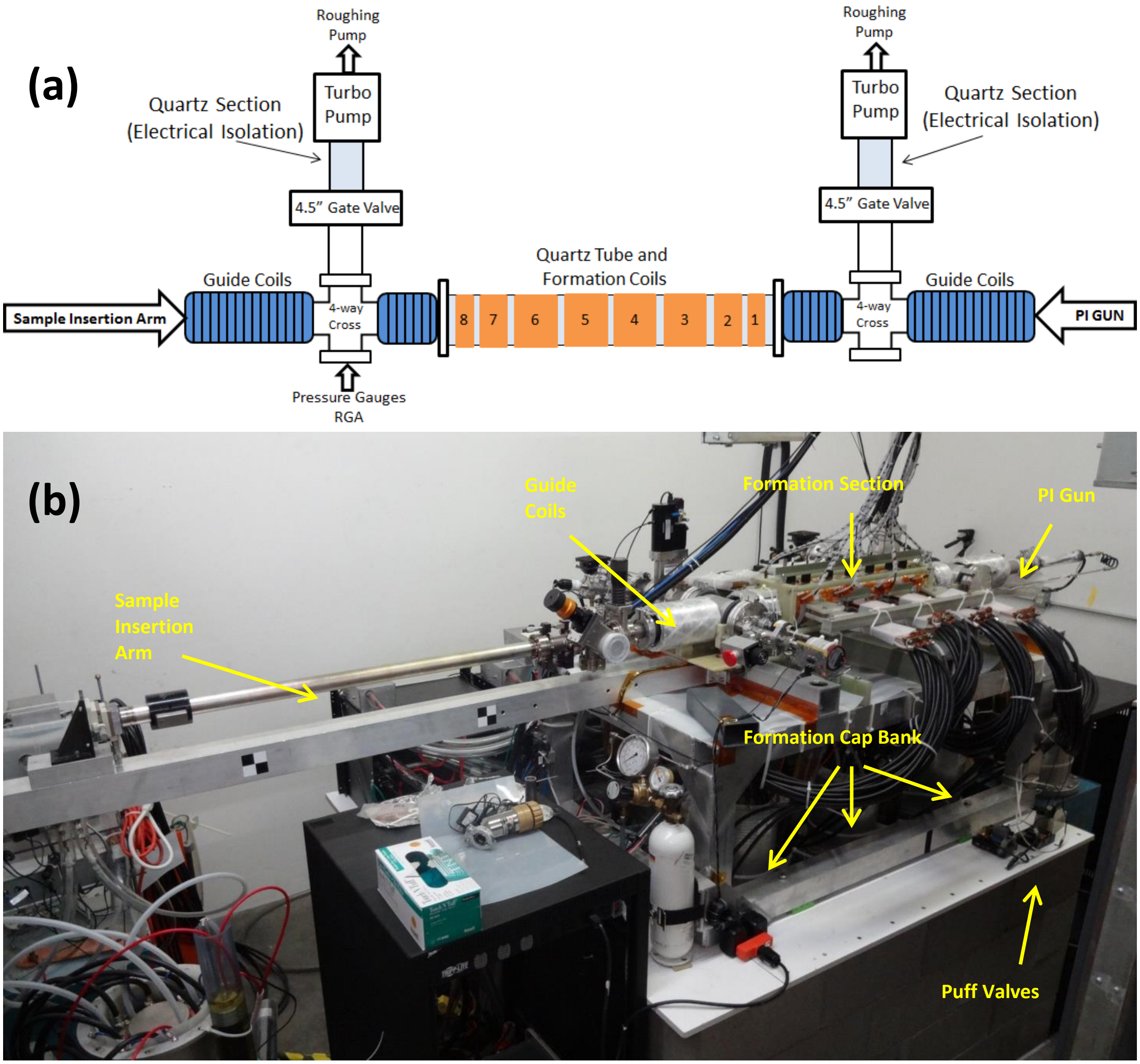

**Figure 2.3: (a) Illustrates the top down view and layout of the FRC chamber with supporting vacuum system. (b) Fully assembled and operational Field Reversed Configuration plasma source designated as plasma-materials interactions studies test bed.**

measured using an SRS RGA 100. Multi-turn, solenoid cusp/guide coils are positioned on each side of the FRC formation chamber to both aid in the formation of the closed magnetic field line profile, and guide the plasma jet onto the sample. Figure 2.1 (a) is a schematic illustrating the top down view of the chamber set up and (b) is a real image of the completed and operational plasma and material exposure chamber. The capacitor charge voltage and related field strengths can be

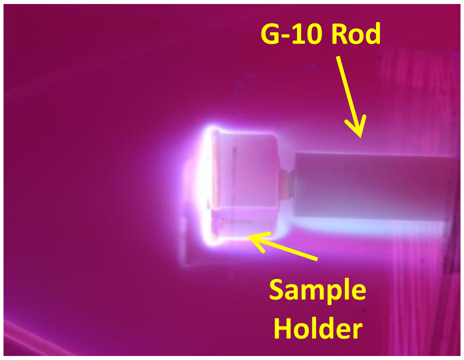

**Figure 2.2: Real image of sample holder set up of G-10 rod holding Macor sample holder. Samples were various types of metals and the image clearly shows a strong interaction with deuterium plasma.**

adjusted to vary the exposure intensity onto the target. These guide coils are typically driven at ~750 V and ~165 Amps with a 1.2 mF capacitor bank having a rise time of 4 ms. This configuration produces a magnetic field strength of approximately 0.2 Tesla. The sample is placed on the end of a standard 4 foot long UHV magnetic translation arm and can be positioned anywhere within the guide coils. A 6 inch section of G-10 is positioned on the end of the magnetic translation arm, and the sample holder screws into the end of the G-10 rod (Fig. 2.2). This is to both electrically isolate the sample as well as prevention of perturbations of the magnetic field lines. On the side opposite from sample insertion, a pre-ionization (PI) gun is positioned. The PI gun is used to aid in the creation of uniform pre-formation plasma within the chamber and is currently operated at 4kV with a local deuterium gas pressure of ~10 mTorr. The PI gun, Figure 2.3, is essentially a series of electrodes arranged in a circular array and initiates plasma production following the Paschen relation of voltage, gas pressure and electrode distance. The fuel gas used to ignite the PI gun is pumped directly into the gun with a controllable puff valve. The quartz tube making up the formation section is surrounded with eight single turn copper coils in a theta-pinch configuration that fit snugly around thin polyethylene shims. Each shim and each coil are individually wrapped with an electrically isolated copper wire loop that will be discussed with more detail in the diagnostics section. The entire assembly is supported by a 0.25 inch thick

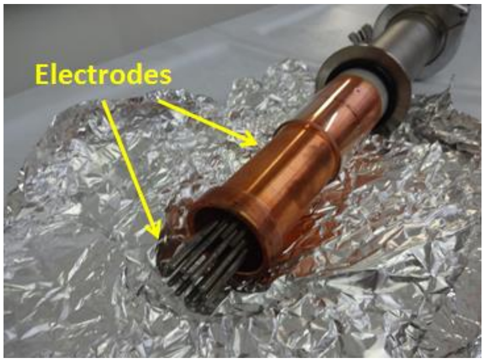

**Figure 2.3: Plasma initiation gun (PI) copper cylinder is one electrode and the circular array of tungsten pins (typically negative) is the other electrode.**

aluminum box frame that sits on top of a 3 foot high cinder block foundation. Housed underneath the aluminum frame and inside the cinder block foundation are the capacitors that make up the formation coil capacitor bank.

## 2.2 Coils and Capacitors

The coils are made from ~1/16 inch thick copper with two electrical feed plates extending from the circular section. Each coil is wrapped in a thin Mylar film for electrical isolation and after the electrical connections are bolted onto the feed plates they are wrapped again with 1/16 inch thick polyethylene sheets. There are 8 coils total, 4 in the middle that are approximately 7 cm wide, on each side of the center 4 there is a 3.8 cm coil and on each end a 2.5 cm coil. This configuration aids to limit field line divergence at the ends of the coil array, because of the higher current densities in the smaller sections, and pinch the ionized gas to form the plasmoid. Figure 2.4 (b) shows how the coils are arranged on the quartz tube with wire loops wrapped around the outer diameter of each coil (flux loops) to measure the magnetic field strength, and (a) is an image of the polyethylene shim with the wire loop (B-loops) wrapped around it that is wedged in between the coil and the quartz tube to measure excluded flux. The feed plate extensions alternate to either side of the formation section to both avoid stress on the quartz tube and to eliminate arching from close proximities of the electrical contacts. The coils are driven by three independent capacitor banks

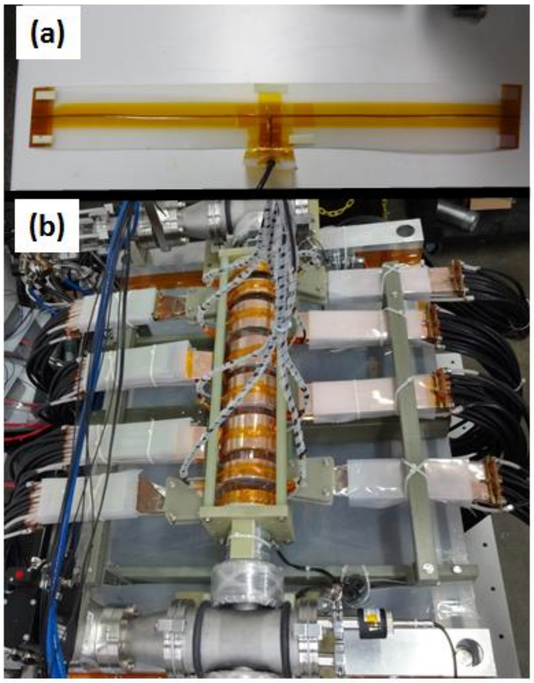

**Figure 2.4: (a) Polyethylene shim with wire loop fastened by capton tape (b) coils in position around quartz tube with wire loops wrapped around the OD to measure B-field strength.**

arranged in a parallel circuit configuration as shown in Figure 2.5a; the main formation bank ($C_F$), ringing-θ ($C_R$) and bias bank ($C_B$). The formation bank is comprised of eight 1.85 µF capacitors each equipped with a 25kV copper-vapor thyratron start switch capable of sub-microsecond triggering resolution. Each start switch is paired with a crowbar switch (CB) that is triggered at peak current, allowing the magnetic field external to the FRC ($B_e$) to remain relatively constant after formation. Each formation capacitor is capable of delivering 150 kA to each coil, generating magnetic field magnitudes on the order of 1 Tesla. The ringing-θ bank (used for pre-ionization) is a 1.8 µF capacitor connected in parallel to the eight formation coils and is operated at 22 kV delivering a ~1 MHz frequency oscillating field profile during pre-ionization. The bias bank is 120 µF inductively isolated (by $L_B$ in Fig. 2.5a) capacitor operated at 4kV providing a 0.1 – 0.2 Tesla negative bias field. Charging of the capacitors is monitored through independent voltage to frequency monitors coupled to a charge control system controlled with Labview. The thyratron switches are mounted directly on top of the capacitors (Fig. 2.5b) with the start switch on the bottom and the crowbar switch on top. The switches are triggered by first heating hydrogen vapor between

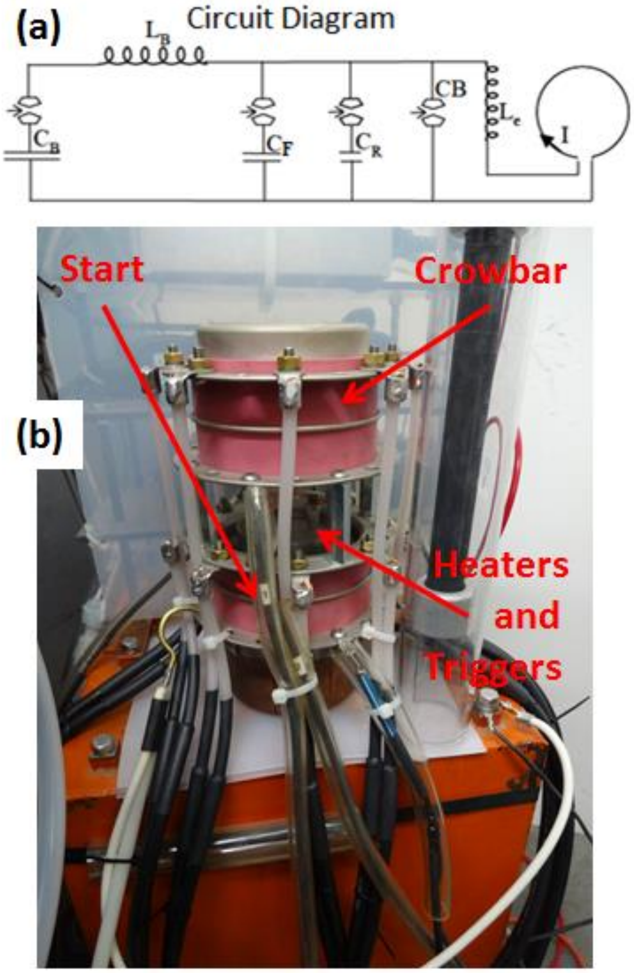

**Figure 2.5: (a) Circuit diagram for each coil showing the bias, ringer, and formation capacitor banks linked in parallel. CB is the crowbar. (b) Is a real image of the standard switch configuration. Switches sit directly on the capacitor (orange).**

two copper electrodes and at the precise time of triggering a pulse is sent into a small electrode on one of the larger electrodes causing a spark that ablates the copper and initiates the conduction across the gap. Each switch has its own heater and trigger which can be adjusted to tune the coils to trigger at highly precise timings.

## 2.3 Controls and Plasmoid Creation

The capacitors and triggering mechanisms are controlled entirely by LabVIEW and the plasma characteristics are retrieved by the various diagnostic systems and plotted for analysis with Matlab. All information relative to the controls and diagnostics are digitized in various ways by devices that are housed in a steel cabinet (DAQ) that sits next to the experiment (Figure 2.6). The cabinet acts as both a ground and insulates the digitizers from stray fields produced by the experiment. The charge monitors, controllers and triggers are fed to and from the experiment via fiber optic cables to reduce interference from the stray electromagnetic fields propagating from the coils. The fiber optic cables are fed into the DAQ via photodiodes that convert the optical signal to a digital signal for controls and data analysis. The plasma diagnostics, PI current and guide coil current are fed into the cabinet through coaxial cables, converted to lemos and into high speed digitizers. Once all signals have been converted to digital they are sent through a standard GPIB module to communicate with LabVIEW and be stored in the local directory.

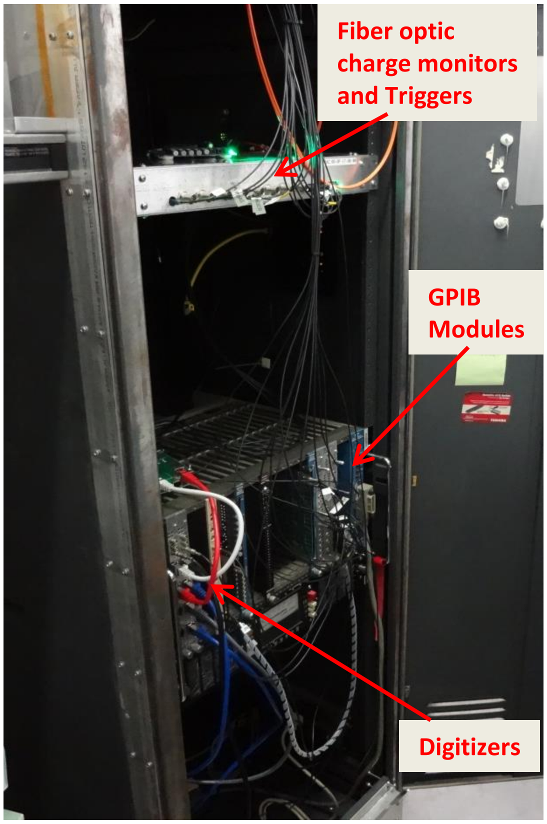

Figure 2.6: Real image of the DAQ cabinet positioned next to the experiment. All signals from the experiment pass through this cabinet as they are digitized.

The pre-ionized fuel gas to be used during the generation of the FRC plasmoid is created through the combination of a bias and ringing field pattern. Fuel gas is pumped into the chamber in two steps; the first puff is timed to fill the chamber to a sufficient fuel gas pressure required for plasmoid formation, fill pressures are typically on the order of 10 mTorr. The second puff is timed to fill the PI gun with enough gas to allow a Paschen breakdown between the gun electrodes at 4 kV. The bias sets the initial direction of the field. The PI gun is then fired providing seed plasma to the formation area. At the first quarter cycle of the bias, the ringing-θ is triggered producing field oscillations that briefly swing the bias field down to zero amplitude to further ionize fuel gas. The formation coils are then triggered rapidly and with the opposite polarity compressing the plasma and reversing field lines resulting in the creation of a closed field plasmoid.  As the plasmoid decays, hot ions flow off the plasmoid, into a jet that streams axially through the guide coils and onto the material target. Figure 2.7 shows the flux loop measurement of the magnetic field under coil number 5, and how the series of capacitor banks, when triggered, result in the characteristic magnetic field pattern that results in the generation of the plasmoid. Table 2.1 is the tabulated values for operational parameters of capacitors used to create the magnetic field profile. The triggering of the formation bank represents time zero and

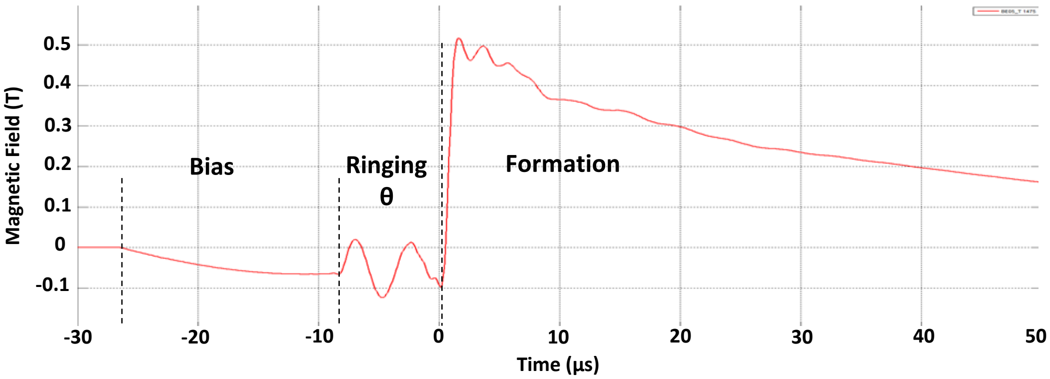

**Figure 2.7: Sample magnetic field profile from B-loop around coil number 5 illustration the characteristic series of events during the creation of FRC plasmoid.**

all other triggering times are relative to the formation bank. The triggering times for the various components of the formation process are critical and in some cases require sub-microsecond scale timing. Thus the requirement that the trigger controllers have the ability to be tuned with such high precision is essential.

**Table 2.1: Values for operational parameters of capacitors used to create magnetic field profiles necessary for plasmoid creation. Formation bank includes eight independent capacitors coupled to their own independent copper coils. Triggering times are in relation to the formation triggering time being set to zero seconds.**

| Capacitor Banks | Capacitance | Charge Voltage | Risetime | Time of Trigger | Field Strength |
|---|---|---|---|---|---|
| Guide coils | 1.2 mF | 750 V | 4 ms | -4 ms | 0.261 T |
| Pre-ionization | 14.7 μF | 4kV | 6.5 μs | -30 μs | N/A |
| Reversed Bias | 122 μF | 4.5kV | 15.7 μs | -26.8 μs | -0.09 T |
| Ringing-θ | 1.8 μF | 22kV | 1.1 μs | -8.5 μs | 0.1 T |
| Formation | 1.8 μF x8 | 20kV | 1.2 μs | 0 μs | 0.8 T |

# 3. Plasma Diagnostics

## 3.1 Compensating Flux Loop Array

The material studies require that the plasma source be well characterized to relate material damage to plasma energies and fluence. This plasma source is characterized through the combination of several fundamental techniques commonly used to measure plasma characteristics. The primary diagnostic technique, a compensating flux loop array, involves the placement of two copper wire loops positioned on the inner and outer circumference of each coil. Using the current driven in each wire loop during magnetic compression, the excluded flux ($\Delta\boldsymbol{\phi}$), and excluded flux radius ($\boldsymbol{r_s}$) of the plasmoid and can be measured and calculated using the following expression.

$$\Delta\boldsymbol{\phi} = \boldsymbol{\pi r_l^2 B_e} - \boldsymbol{\phi_l} = \boldsymbol{\pi r_s^2 B_e} \qquad \text{eq. } \mathit{3.1.1}$$

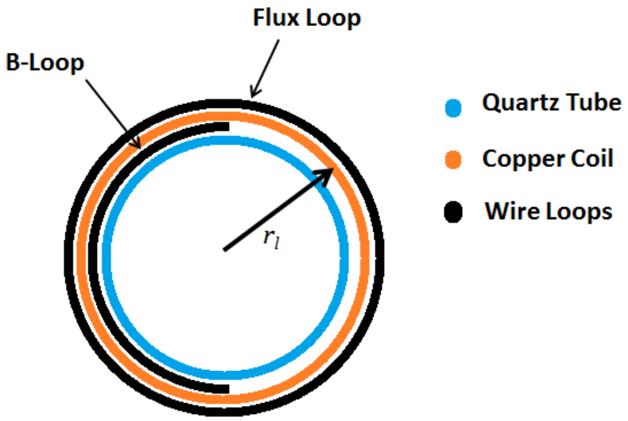

**Figure 3.1: Drawing illustrating the flux loop and B-loop placement used to measure magnetic field and excluded flux.**

Here the loop surrounding the OD of the coil measures the total flux ($\boldsymbol{\phi_l}$) and ($\boldsymbol{r_l}$) is the radius of the flux conserving area. The crescent shaped loop surrounding the polyethylene shims measure the portion of flux that is compressed against the coils as the plasmoid is formed. Figure 3.1 is an illustration of the cross section of the formation chamber and shows hoe the two wire loops are positioned. The total flux can be measured by the flux loop wrapped around the coils by integrating the voltage $V_f = d\phi/dt$, the flux resulting from the diamagnetic response of the plasmoid can be measured by the integrating the voltage in the B-loop wire $V_b = d(A_b B_e)/dt$, where $A_b$ is the internal area of the crescent shaped B-loop which is really the length and thickness of the polyethylene shim. Assuming $B_e$ is uniform, the excluded flux is the difference

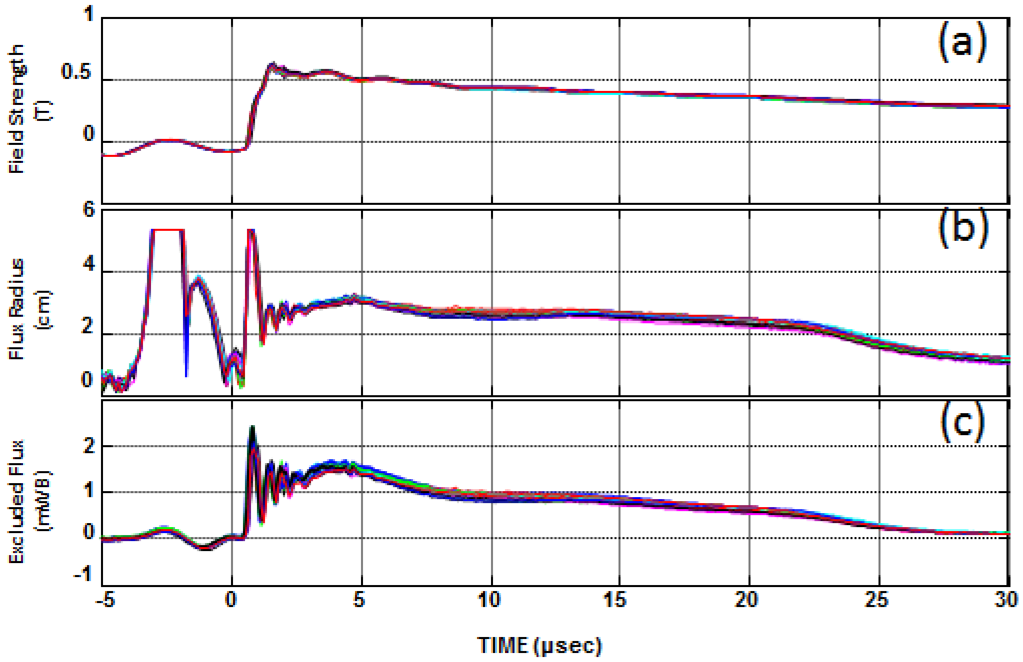

**Figure 3.2: Compensating flux loop array data from coil five. (a) magnetic field, (b) exluded flux radius, (c) magnidude of excluded flux.**

between them. Each coil is fitted with B-loops and flux loops so that entire shape of the plasmoid can be characterized. Figure 3.1 is an example of measurements taken from compensating flux loops on coil number 5, which is roughly in the center of the formation section. Graph (a) shows the magnetic field strength, (b) is the excluded flux (plasmoid) radius and (c) the excluded flux field strength. It can be seen that over the course of 15 consecutive shots the magnetic field and plasmoid excluded flux conditions remain highly consistent and give rise to a plasmoid cross sectional radius of ~3.5 cm with a life time of on average ~25 μs. From the data collected on all coils it was determined that the plasmoid lengths are averaging approximately 40 cm. It was observed that these conditions can be further sustained over the course of hundreds of shots. Figure 3.2 is an example of measurements taken from compensating flux loops on coil number 5, which is roughly in the center of the formation section. Graph (a) shows the magnetic field strength, (b) is the excluded flux (plasmoid) radius and (c) the excluded flux field strength. It can be seen that over the course of 15 consecutive shots the magnetic field and plasmoid excluded flux conditions remain highly consistent and give rise to a plasmoid cross sectional radius of ~3.5 cm with a life time of on average ~25 μs. From the data collected on all coils it was determined that the plasmoid lengths are averaging approximately 40 cm. It was observed that these conditions can be further sustained over the course of hundreds of shots.

### 3.2 Interferometer

With the plasmoid radius known, a Michelson Interferometer was used to measure the density of plasma in the center of the plasmoid. One beam of the laser is passed through the formation section between coils 4 and 5, the reference beam is passed over the top of the coils and back to recombine with the first beam where the co-linear beams constructively and destructively interfere depending on their relative phase shift. The frequency of the laser should be chosen to avoid any absorption from the bound electrons that would change the refractive index compared to the free electrons in the plasma. This is important as it is the interaction between the EM field of the laser with the free electrons in the plasma that cause a phase shift in the laser light as it passes through the plasmoid. From the change in phase ($\Delta\boldsymbol{\varphi}$) between the split beams the plasma density can be calculated using the following relation [7].

$$\Delta\boldsymbol{\varphi} = \frac{\boldsymbol{\omega}}{\mathbf{2}\boldsymbol{c}\boldsymbol{n}_{\boldsymbol{c}}}\int \boldsymbol{n}_{\boldsymbol{e}}\boldsymbol{dl} \qquad \text{eq. } 3.2.1$$

where $\omega$ is the angular frequency of the laser, $c$ is the speed of light, $n_c$ is the cut-off density related to the plasmas index of refraction, $dl$ is the path length through the plasma or in this case the cross sectional diameter of the plasmoid, and finally $n_e$ is the electron density which for deuterium is equal to the ion density. The interferometer is not in a standard Michelson configuration in that the probe beam only passes once through the plasma (Fig. 3.3), however the beams can be tuned for alignment through the use of several adjustable mirrors and oscilloscope just before the beams enter the photodiode in the sampler. By employing this technique, it was determined that plasma densities are averaging ~$5 \times 10^{21}\ m^{-3}$at 10 μs during the plasmoid equilibrium stage. In addition, from the density and field measurements it was determined that the plasma temperatures are averaging ~130eV.

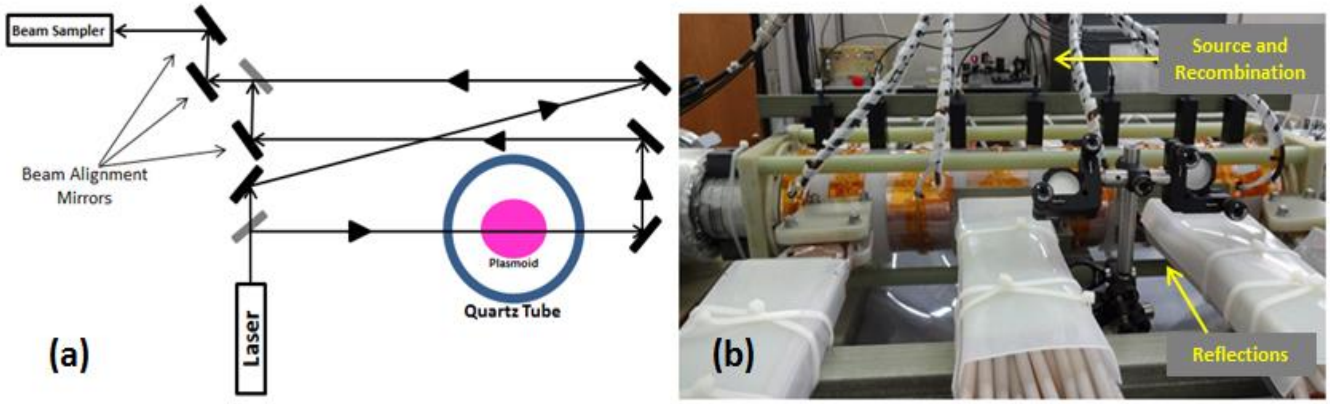

**Figure 3.3: (a) schematic showing the interferometer configuration and (b) real image from the experiment with the beam source and recombination platform in the background sitting on a stage that reduces**

### 3.3 Pressure Probe

Traditionally ion velocities are measured with a Langmuir probe. However, because the ion energies far exceed the work function of valence electrons within tungsten probe material a Langmuir probe may not yield accurate information to determine average ion velocities within the plasma jet. Following a previous design, outlined by S.J. Messer et.al. [8] , a novel design making use of a dynamic pressure probe was used to measure ion velocities in sample exposure positions within the plasma jet. The probe utilizes a PCB Piezotronics model 113B21 pressure sensor modified to work in the plasma jet environment. The entire probe was housed within a 1 cm OD, 0.7 cm ID, 122 cm long quartz tube using a low vapor pressure epoxy for a vacuum tight seal. The probe was positioned in the tube such that the sensor end protrudes from the end of the tube approximately half of a centimeter. The sensor itself has a stainless steel casing; therefore, it was necessary to isolate the protruding part of the probe from the conductive plasma by applying a thin layer of epoxy around all exposed surfaces. A boron nitride annulus was positioned around the end of the quartz tube to allow the sensor end to be exposed directly to the plasma while protecting the epoxy seal from the plasma jet. Additionally, tungsten foil was attached to the leading edge of the sensor with an extremely thin layer of epoxy to absorb the direct energy of the plasma without damping the sensitivity. Figure 3.4 illustrates the probe and corresponding dynamic pressure waveform during operation. The sensor was tested before and after the

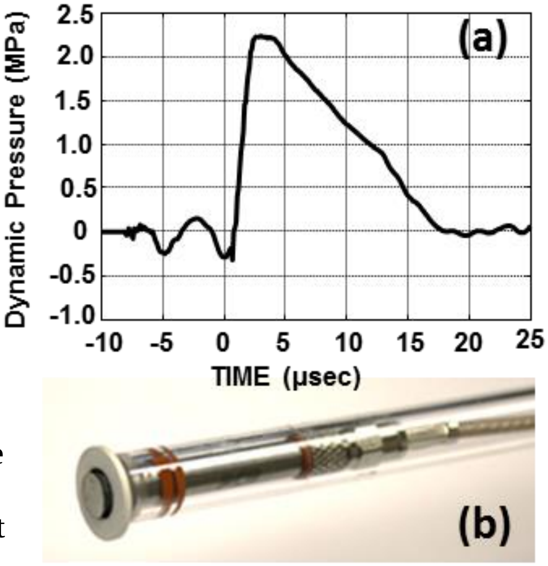

**Figure 3.4: (a) Typical Pressure vs. Time plot for dynamic pressure wave of plasma jet. (b) Real image of probe inside quartz tube with boron nitride annulus surrounding the sensing surface.**

modification and it was determined that there was no sufficient change necessary in the factory calibration of 3.6mV/kPa. The relation between pressure and ion velocity is expressed by the following:

$$\boldsymbol{P_0 = n_0 kT = 0.5\rho v^2} \qquad \text{eq. } \mathit{3.4.1}$$

where $P_0$ is the pressure, $\rho$ is the mass density of a deuterium ion, and $v$ is the ion velocity. As a result, measurements indicate dynamic pressure readings on the order of 1MPa at 10 μs which translate into ion velocities on the order of ~300 km/s at the sample exposure position. With the ion velocities and densities known it was determined that the average fluence per shot is on the order of 1MJ/m$^2$.

### 3.4 Plasma Jet Diameter

In order to prepare samples or place multiple samples in samples on a holder it is important to know the cross sectional of the plasma jet where the energies are highest. In an effort to do so X-ray photoelectron spectroscopy (XPS) was employed in an attempt to map the structure of the plasma jet in sample exposure positions. It has been seen in our previous studies through extensive XPS analysis that deuterium plasma has sufficient energy to facilitate carbon-silicon bonding on the plasma facing surface of silicon rich Macor samples [9]. These studies showed that atmospheric carbon deposited on the surface of macor samples before insertion into the FRC chamber resulted in a substantial formation of silicon carbide. Therefore, a flat Macor disk was polished, and prepared for deuterium exposure

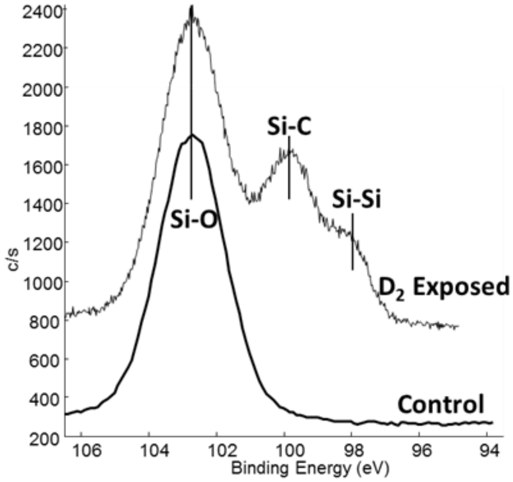

**Figure 3.5: X-ray photoelectron spectroscopy results from Macor target before and after deuterium plasma exposure. The control samples shows 100% oxidation of silicon constituents whereas the exposed sample clearly shows the addition of carbide and silicon segregation on the surface**

by sonicating the sample in both methanol and isopropanol for 15 minutes each. The sample surface was allowed to be exposed to atmosphere before being placed into the FRC chamber allowing for a uniform thin film of atmospheric carbon contamination to be deposited onto the surface. Figure 3.5 is an example of the XPS surface scans comparing the unexposed control sample of Macor with the deuterium irradiated sample. It can be seen that in the control sample the silicon exists only in the oxidized state, however the deuterium exposed sample shows the addition of two distinct new peaks. One at the binding energy of 99.8eV, a characteristic binding energy for silicon carbide, and another at 98.0eV implying some silicon segregation has occurred on the surface as a result of the exposure. It was proposed that during exposure the variance in the energy cross section of the ion beam should result in an identical chemical pattern of silicon carbide formation on the Macor surface. Therefore, extensive XPS and depth profiling analysis was performed by scanning a cross section of the Macor sample surface after exposure. Analysis focused primarily on the Silicon 2p peak. Specifically, the percentage of oxide, carbide and silicon segregation was measured at 2 mm intervals across the sample surface. Results from the analysis can be seen in Figure 3.6. It appears that the silicon carbide is most prevalent in the center of the sample and is consistent

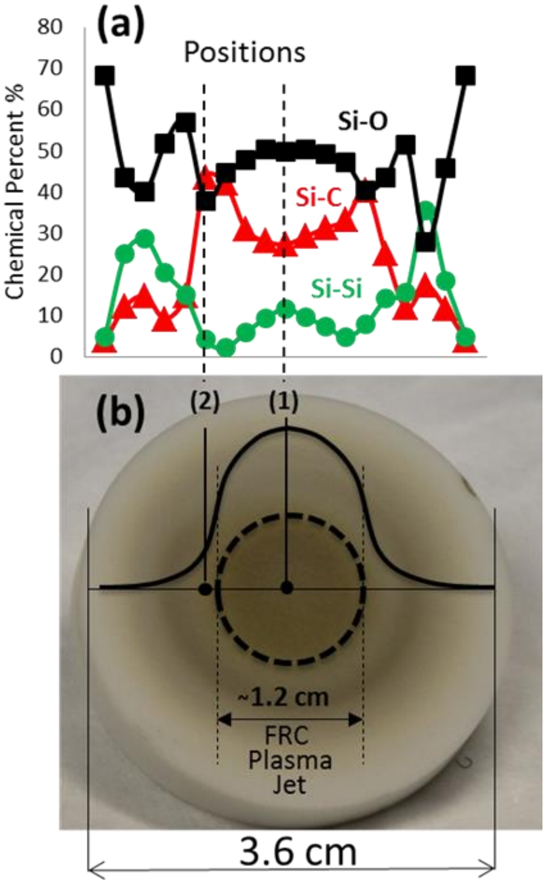

**Figure 3.6: (a) XPS surface analysis of chemical percentages in the silicon 2p peak and (b) Macor target with circular discoloration patterns associated with the deuterium plasma jet and superimposed Gaussian beam**

with the visible discoloration at the samples center. The variance in the chemical percent was low in the central 1.2 cm of the sample and a sharp increase of silicon carbide was detected at the edges of this central region. XPS depth profiling was then conducted in the center position and at the edge of the 1.2 cm structure with a low energy argon sputtering technique. Analysis of the depth profiles focused on the carbon 1s peak. Figure 3.7 illustrates the results from the depth profiling of the center (position 1) and the outer edge of the inner ring structure (position 2). It appears that the carbide in the center position was more persistent and harder to remove than the outer edge implying a deeper penetration of carbon into the material from a more energetic region of the plasma jet. The edge of the inner ring structure shows a higher percentage of carbide, but was easier to remove which would be more consistent with a carbide deposition from the sputtering of the center during the exposure. As a result the size and structure of the plasma jet could be mapped at a spacial resolution of 2 mm. Theoretically the resolution could be as low as the XYZ axis manipulator resolution on the stage of the XPS which is less than 0.5 mm. Figure 3.6(b) is an image of the Macor disk after 100 shots and clearly illustrates the circular and symmetric nature of the plasma jet with the superimposed results of the plasma beam energy profile from the XPS depth profiling study. It was concluded that the beam structure was Gaussian with a FWHM of approximately 1.2 cm.

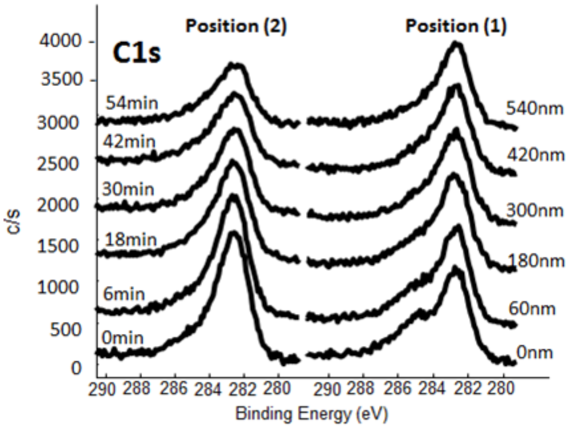

**Figure 3.7: XPS depth profiling results . Center (position 1), outer edge (position 2). Indication that in the center position the carbon atoms where driven deeper into the material resulting from higher plasma jet energies.**

# 4. Material Exposure and Analysis

## 4.1 Overview of Material Studies

Our preliminary studies focused on two broad areas of interest; the effects of chamber geometry on sputtering and re-deposition, and chemical as well as morphological changes resulting directly from wall exposures to pulsed plasmas. Although the long range goal of our experiments will investigate a variety of plasma fuel gasses, Hydrogen through Xenon, our preliminary studies involved the use of high density deuterium plasma with an average energy fluence ranging from10kJ/m$^2$ to 1MJ/m$^2$. The primary metal materials to be tested were; copper, aluminum, zirconium, titanium, tungsten, and the ceramic materials of interest where Macor [9] and Beryllium Oxide. These materials were chosen for their intrinsic properties such as electrical and thermal conductivity, hardness and resistance to sputtering, and resistance to ion and neutron implantation. Macor was used as the sample holder during exposures for its insulating properties, low thermal conductivity and coefficient of thermal expansion, as well as chemical stability and composition. The composition of Macor is known to include silicon, magnesium, aluminum, potassium, boron, and fluorine. With the exception of fluorine, all other elements present in macor are in oxidized form, therefore, by employing macor as the sample holder we were able to introduce a ceramic sample as well as additional metals for chemical analysis during our exposures.

Effects of geometry on the sputter and re-deposition dynamics during pulsed plasma exposures were conducted by setting the metal specimens in the macor sample holder at varying heights and depths relative to the holder surface. The samples were observed before and after exposure using both optical microscopy (OM) and Scanning Electron Microscopy (SEM). In this context OM and SEM imaging were deployed as a tool to provide a visual representation of the resultant degree of sputtering and re-deposition of samples in the Macor holder. As well X-ray photoelectron spectroscopy (XPS) was used to identify which elements and relative amounts were re-deposited onto both the samples and the macor holder. The information obtained through OM, SEM, and XPS were used to develop a qualitative and quantitative model dictating the importance of position within the chamber on sputter and re-deposition phenomena which includes identifying the thickness of the sputter re-deposition layer on the surface of Macor and the relative thickness of the deposition layers as a function of sample height was clearly indicated through XPS analysis with an argon sputter depth profiling method..

Furthermore, chemical and morphological interactions between plasma and sample materials were analyzed primarily through SEM, EDX and XPS. In this context the ionization affects, chemical reactivity, and oxidation states of a variety of materials exposed to deuterium plasma were observed. Formations of carbides on tungsten and zirconium substrates were seen, the chemical composition of depositions was determined. SEM and EDX images revealed slight changes in morphology on some sample surfaces such as localized oxide formation, preferential sputtering and in some cases surface structures that were unique to the substrates elemental composition.

## 4.4 Macor Study

Macor is a machinable glass ceramic commonly used in industry. It has a low coefficient of thermal expansion, good dielectric properties and is chemically stable up to 1000°C. It is a combination of fluorophlogopite mica in a borosilicate glass matrix. Its usefulness as an electrical insulator and its composition, which involves the combination of several metal oxides, make it an ideal material to study under the extreme conditions of the plasma chamber.

Therefore a sample of Macor was prepared and exposed to 100 shots of deuterium plasma at an energy fluence of ~10kJ/m$^2$ per shot. The exposed sample was compared to the control first by a visual inspection with low resolution optical microscopy. The exposed sample was slightly discolored with a light yellow discoloration and when viewed under the microscope the exposed sample was much more rough and glassy. When viewed under the microscope the control sample has a brilliant white color and sparkles because of the presence of phlogopite crystals. The exposed sample showed no visible signs of crystal reflections on the surface, instead it has a pale uniform color. This result is consistent with what would be expected as the recombination of the surface resulting from the bombardment of high temperature deuterium would result in an amorphous glass microstructure. Further analysis with XPS revealed two interesting results.

First it was noticed that the fluorine 1s peak is substantially reduced on the surface of the exposed sample (fig. 4.1). Fluorine is primarily found in the phlogopite mica crystals and is typically bound to the potassium atoms within the interatomic planes of the mica structure. It is what gives strength to the interatomic planes and is fundamentally responsible for the machinable properties of Macor in general [10]. This can be explained by two fundamental chemical processes. One possibility is that the deuterium exposure results in the formation of deuterated fluorine (DF) in the bulk and sputter re-deposition sheath. When it is re-deposited onto the surface it effectively etches away the silica and results in the formation of

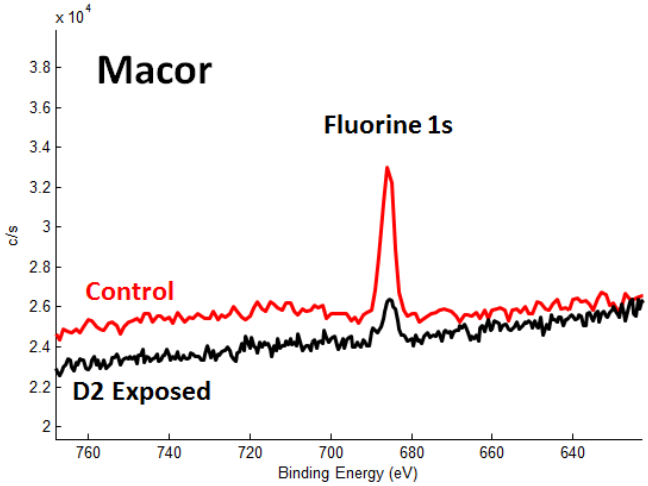

**Figure 4.1: XPS spectrum of fluorine 1s peak showing a substantially reduced presence of fluorine in the deuterium exposed sample.**

tetrafluorosilane ($SiF_4$) and is evolved from the material surface as a gas described by the chemical equation:

$$\boldsymbol{D^+ + F^- \rightarrow DF} \qquad \text{eq. } 4.4.1$$

$$\boldsymbol{4DF + SiO_2 \rightarrow SiF_4 + 2D_2O} \qquad \text{eq. } 4.4.2$$

this combination of chemically induced desorption results in the removal of most fluorine on the surface and to some extent into the bulk depending on the penetration depth of the deuterium.

Another interesting result from the XPS data is the segregation or reduction of silicon on the surface. It can be seen in the XPS spectra (fig. 4.2) that pure silicon is being formed during the exposure. Assuming most chemical mutations are occurring in the sputter sheath because of the presence of both free ionized single elements or ionized particles, most reactions should occur in order of their thermodynamic properties. This would result first in the formation of deuterated water. The formation of water would result in oxygen depletion as the sputtered elements are re-deposited onto the surface. Thermodynamically magnesium and aluminum have a higher affinity to re-oxidize before silicon, therefore it is reasonable to expect to see only reduced silicon in the XPS spectra and not reduced magnesium or aluminum, which is exactly what is seen in the spectra.

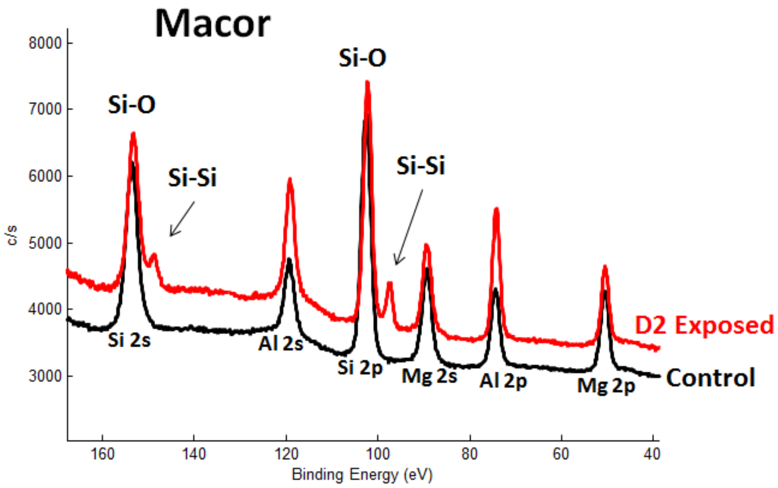

**Figure 4.2: XPS spectra of control and deuterium exposed sample. The reduction of silicon can be seen in the exposed sample and no reduction of magnesium or aluminum can be seen.**

## 4.3 Metals Study

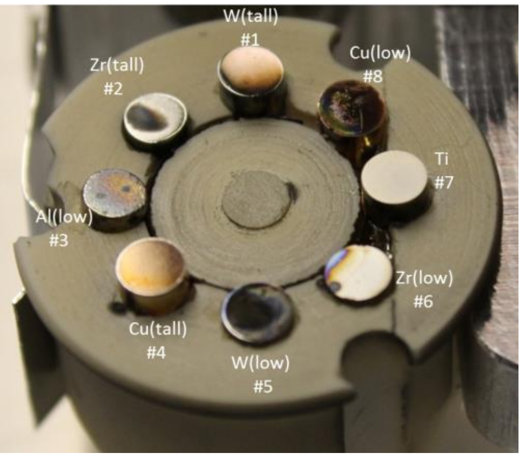

**Figure 4.3: Metal pellets of varied elemental nature in MACOR sample holder just after deuterium exposure**

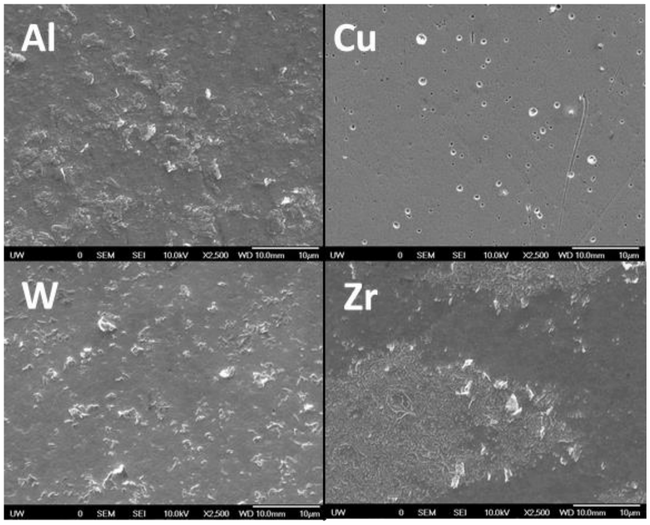

**Figure 4.4: Surface images from four different materials exposed to deuterium plasma at approximately 10kJ/m$^2$.**

The second study was conducted to evaluate chemical and morphological effects of various metals exposed to deuterium plasma. In this study macor was again employed as the sample holder. The samples included copper, aluminum, tungsten, titanium, and zirconium. Figure 4.3 is a photograph taken just after exposure and illustrates the sample configuration. In this experiment the tungsten (W), copper (Cu), and zirconium (Zr) samples were set at two heights relative to the holder surface for both a strong and weak interaction with the macor. There was only a single sample of both aluminum (Al) and titanium (Ti) set at intermediate heights. The Al sample was visibly the most damaged by the exposure. OM images confirmed the presents of well rounded edges and large cracks on the surface of the Al sample. The Ti sample was visibly the least affected by the exposure. Later XPS analysis of the Ti sample indicated that a thick deposition of Zr had been deposited on the surface with little presence of macor material. SEM was used to further explore the morphological effects of the deuterium exposure on the plasma facing surfaces. Figure 4.4 is a collection of SEM images from the Cu, Al, W, and Zr samples at 2500 times resolution. The Al and W samples have a similar morphology in that there seems to be a rather uniform pattern of oxide formation. EDX was used to confirm that the formations are in fact oxides; however due to the presence of oxygen in the macor it is unknown as to whether the formations oxidized during the irradiation or after being exposed to atmosphere. The Cu and Zr samples have a rather unique morphology. The Zr sample has a non-uniform visible appearance. The darker regions indicate a smother surface whereas the lighter regions a considerably more rough. Although EDX confirmed the existence of both carbon and oxygen in both regions it was not conclusive in the chemical nature of bonding in both regions. In the case of Cu, the exposure caused micron sized pits to form all over the surface of the sample. Using EDX the pits were found to be copper oxide formations and seem to increase in number toward the edges of the sample. Figure 4.5 illustrates how the pitting becomes more pronounced at the edge and is consistent with the deposition findings in part one of the analysis. This would indicate that for protruding elements of the chamber design the edges will experience a significantly stronger physical interaction with the plasma. The image also shows regions of low oxidation (dark region enclosed by circle), and high oxidation (light region enclosed by circle). It is unknown whether this is a direct affect of the deuterium exposure but it’s interesting that they are essentially side by side. XPS scans were run on all samples. In the case of Zr it was determined that the presence of carbon on the surface of the Zr sample deposited as a result of exposure to atmosphere before the sample was irradiated with deuterium may have resulted in the formation of zirconium carbide. An argon depth profiling study was conducted on the Zr sample. After 5 minutes argon sputter the macor

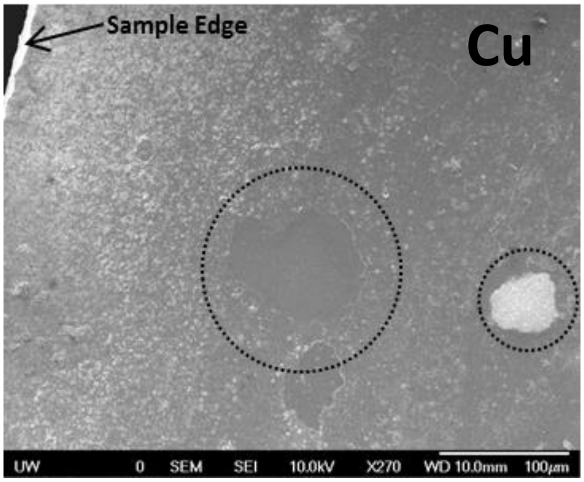

**Figure 4.5: SEM image of copper after deuterium exposure. Surface pitting becomes denser on the edges.**

deposition layer was significantly removed revealing high intensity Zr peaks that were centered in position consistent with metallic Zr; however, upon inspection of the carbon 1s peak, Figure 4.6, it was seen that a small amount of graphitic carbon still remained after 5 minutes sputter as well as a possible zirconium carbide peak centered at 282.1 eV. The NIST standard for C 1s ZrC is between 281.1eV and 282.1eV, this is consistent with our results. It is possible that the exposure to high energy deuterium was the catalyst for the formation of ZrC on the surface of the sample. The sample was further sputtered for a total of 30 minutes and it was observed that the graphitic carbon was quickly removed leaving only the carbide that seemed to be highly resistant to sputtering.

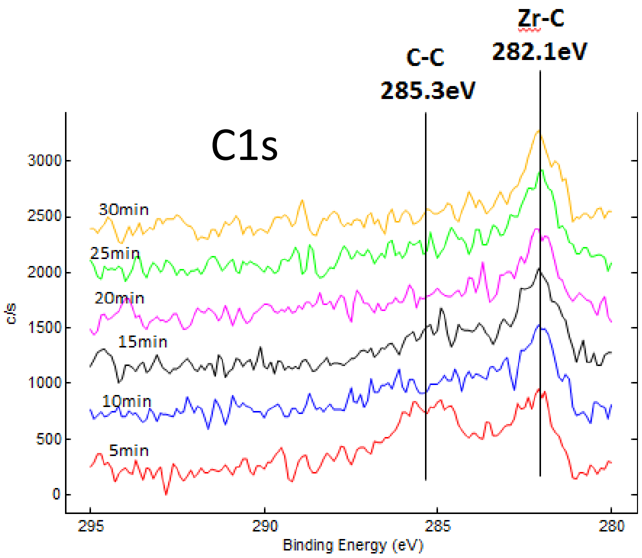

**Figure 4.6: XPS depth profile study showing the existence of zirconium carbide after the pellet was exposed to deuterium plasma.**

### 4.2 Sputter Sheath and Redeposition Study

These experiments were carried out in an ex-situ technique where samples were exposed to atmosphere before and after deuterium exposures. The consequent contamination of atmospheric gasses provided a source of carbon for the creation of carbides, however, due to the presence of oxygen in the macor, atmospheric contamination of oxygen would have played a less significant role on the chemical nature of the post exposed samples. A pulsed laser deposition of macor was conducted to compare with the plasma induced deposition. It was seen that both depositions were fairly similar, although a close inspection of XPS scans seem to indicate wider peaks in the pulsed plasma deposition corresponding to a larger variety of oxidation states and amorphisity of deposited layers. Further in-situ experiments will be carried out with samples being contained within high vacuum conditions to eliminate atmospheric contaminants.

In the first experiment tungsten pellets were used to gauge sputter and deposition effects from the plasma exposure. The macor, with a variety of constituent elements, serves as a good indicator as to average sputter and re-deposition dynamics for a broad range of insulating materials. Each tungsten pellet was placed into the macor sample holder at different depths and heights relative to the holder surface. Figure 4.7 illustrates the pellet arrangement for the experiment. Two pellets were recessed into the holder at -1/16” and -1/32”, one sample was flush and one slightly above the surface (<+1/32), and three above the surface at +1/32”, +1/24”, +1/16”. As expected, the deposition was greatest near the macor surface and decreased with distance. In this discussion, for simplicity, we will omit the data for samples -1/32”, and +1/32” as they follow the observed pattern and are not necessary. Figure 4.8 represents the optical images and XPS scans of tungsten samples taken just after exposure was complete.  It can be clearly seen that there is a substantial difference in physical appearance as well as in the XPS spectrums between all samples. The tallest sample (+1/16”) in both the OM image and the XPS scan seems to have a very thin deposition. Because the tungsten peaks are strong this is an indication that the deposition is well under the standard X-ray sampling depth of 10nm. The next tallest sample at +1/24” is starting to show visual signs of discoloration due to deposition of macor material; however the XPS scan still shows a strong tungsten signal again indicating the deposition is under 10nm thick. The sample that was just above the surface (<+1/32) is visually the most extreme in discoloration. As indicated by the

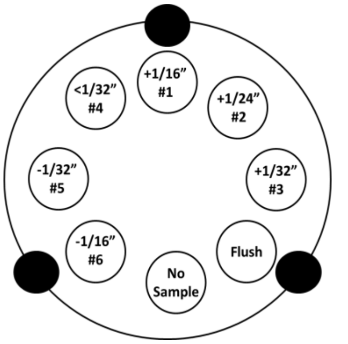

**Figure 4.7: Positions of metal pellet samples in MACOR holder during deuterium plasma exposure.**

intense coloration the sample seems to have a heavy deposition around the perimeter of the sample and seems to taper off in thickness toward the center. The XPS scans show little if any signs of the tungsten substrate, therefore the deposition should be at least 10nm thick. The flush sample also shows strong visible signs of macor deposition. Again we see the heavier deposition around the perimeter tapering off toward the center, but looking at the XPS scan we can see that there is a small tungsten signal, therefore the deposition is close to 10nm. The recessed sample shows an interesting, although predictable, result. There is clearly a macor deposition; however

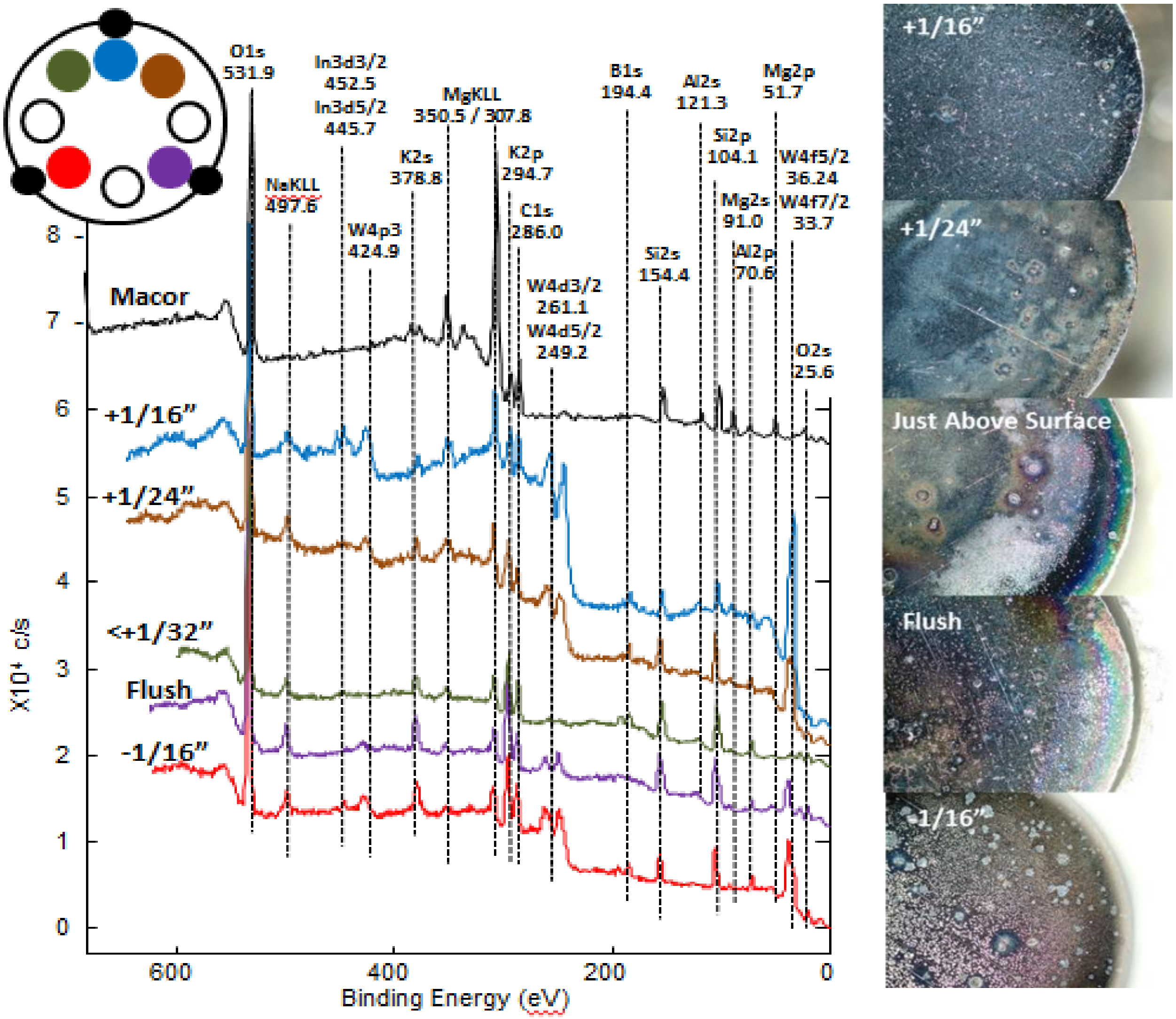

**Figure 4.8: XPS spectra for metal pellets at varied heights relative to MACOR sample holder surface (left). Optical images of tungsten samples after deuterium exposure showing varied degrees of MACOR deposition on the surface.**

the visual appearance is noticeably different than the exterior samples. The deposition seems to be thicker in the center rather than at the perimeter which makes sense as the recessed sample would restrict the plasma flow to the center due to the walls. It's a well-known phenomenon that fluorine evaporates out of macor when it's under high vacuum conditions. However the largest peaks seen in all sample XPS scans indicate that potassium and silicon contribute to the largest portion of the deposition. Interestingly potassium oxide makes up only 10% by weight of the macor composition where silica makes up 46%, yet the peaks are almost equal in intensity. Magnesium oxide makes up 17% of the macor composition but it had the lowest signal strength in the scans indicating it may have the lowest sputter rate. Through this study it was determined that the redeposition sheath extends approximately 2 mm from the surface of the sample holder at energy fluencies of ~10kJ/m$^2$ and subsequent exposures should take this into consideration. The following model (fig.4.9) further illustrates the different morphologies of the re-deposited Macor onto the surface of the tungsten pellets as a function of height and physical location relative to the surface of the sample holder.

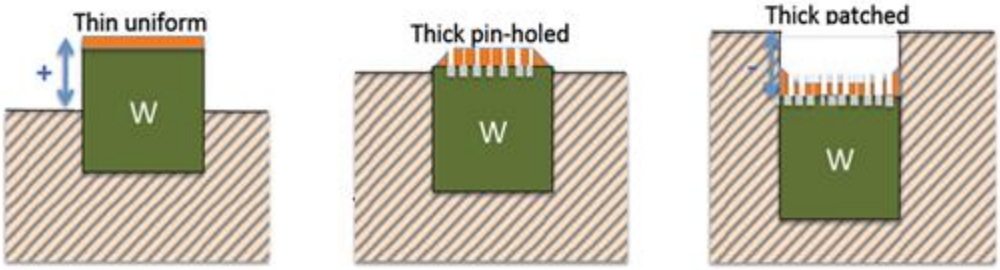

**Figure 4.9: Physical model showing the different ways that Macor was re-deposited onto the surface of the tungsten pellets as a function of height or physical location relative to the surface.**

## 4.5 Beryllium Oxide Study

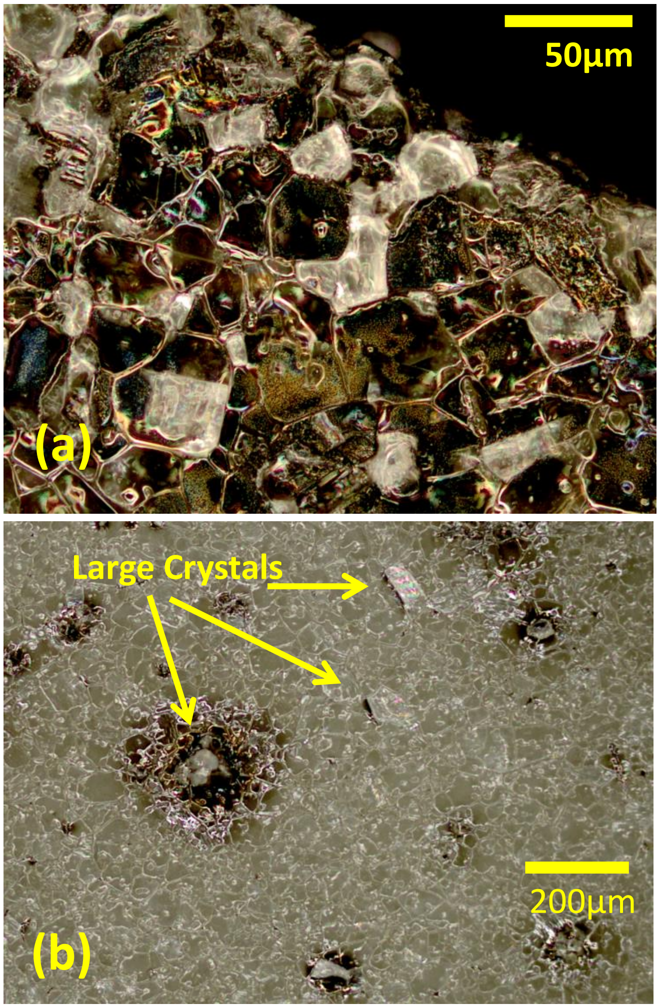

**Figure 4.10: Optical images of beryllium oxide post exposure to deuterium plasma. (a) 20X magnification showing damaged to some crystals indicated by darker regions and (b) 5X magnification showing signs of crystal growth.**

Beryllium oxide is a good candidate for plasma facing positions in high density plasma environments [11]. Particularly for nuclear fusion power production as it has high thermal conductivity, high strength, and beryllium can undergo nuclear transmutations that result in the formation of tritium and would therefore serve as a fuel gas breading blanket. A 99.9% pure sample of BeO was donated to the research group by Materion for study. The sample was exposed to 100 shots of deuterium at ~1MJ/$m^2$ per shot. Optical microscopy and XRD were performed on the sample with clear results. Heavy damage to the material can be seen in the optical images (fig. 4.10a). However, some crystals seem to be unchanged by the exposure and in some cases it appears the crystals have grown larger (fig. 4.10b). In the images the darker regions indicate the areas damaged the most in the exposure and the lighter areas are less affected. In figure 4.10a it can clearly be seen that in an area with heavy damage there are some crystals that remain unaffected, and in figure 4.10b it can be seen that some crystals have grown larger and in heavily damaged spots it appears there are crystals growing out of the center giving it a fuzzy blurred

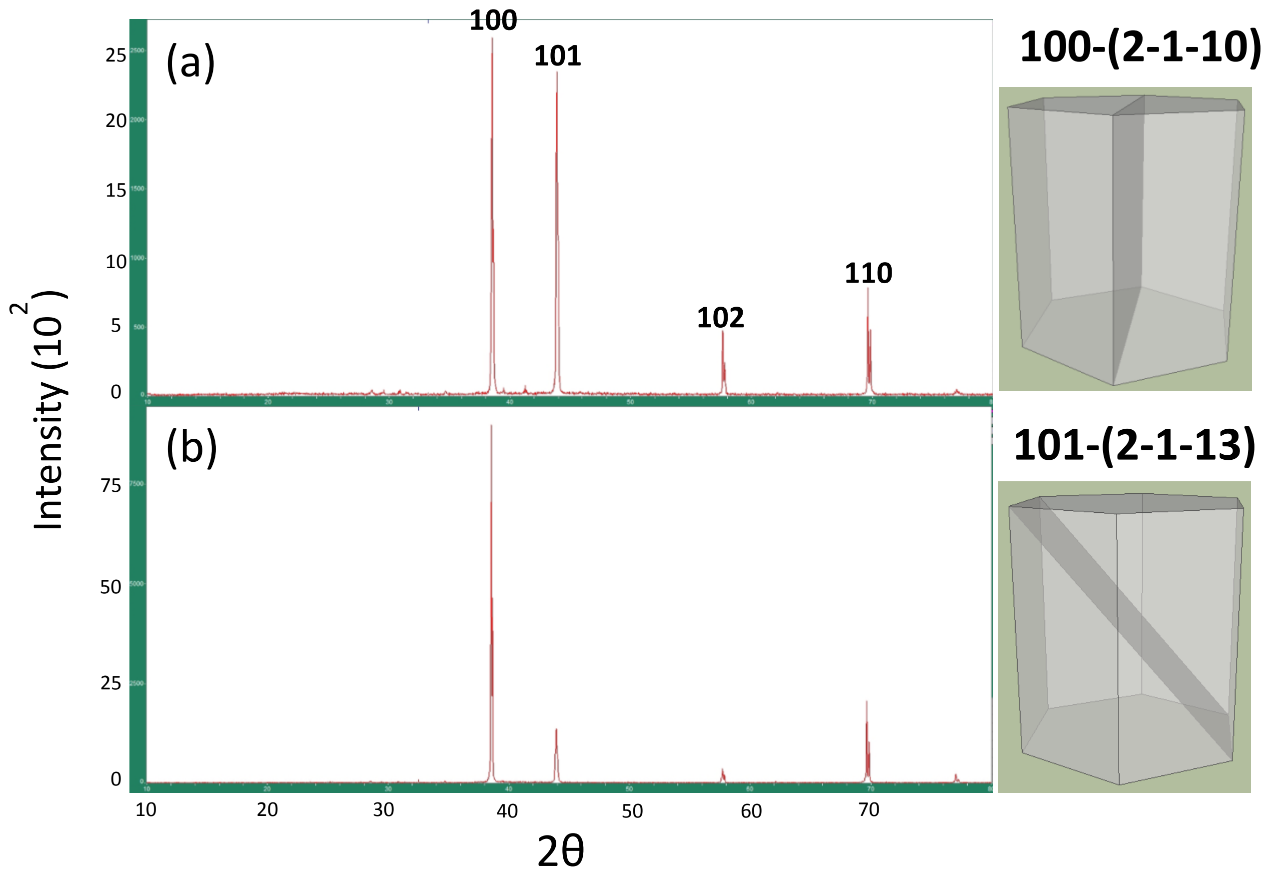

**Figure 5: XRD spectra for (a) the control sample and (b) the exposed sample. To the right are illustrations of the relation between peak indices and crystal planes.**

appearance in the optical images.  Further analysis was performed with XRD. Although there was no conclusive evidence that showed signs of lattice expansion resulting from deuterium implantation during the plasma exposure, there was a significantly large change in the relative peak intensities compared to the control sample. It can be seen in the XRD spectra for the control sample (fig. 4.10a) that the primary peaks are the 100 and 101 which represent the (2-1-10) and (2-1-13) hexagonal crystal planes respectively. In the exposed sample the 101 and 102 peaks are significantly reduced and in fact the 100 peak shows a drastic increase in its intensity. This implication of the results from both optical microscopy and XRD are that the 101 and 102 crystals are being preferentially sputtered or destroyed in the exposure and that there may even be crystal growth in the 100 orientation. It is possible that as the exposure is taking place the crystal structure in the 101 and 102 orientations is being destroyed on the immediate surface effectively changing the index of refraction. That could explain why the grain boundary can still be seen but there is much more optical absorbance on the surface giving it a dark image. This would also be consistent with the XRD results that show a decreased presence of crystal structure in that orientation. Furthermore as the sputtered beryllium and oxygen return to the surface they effectively become building material for the 100 crystals during the high temperature cycle of the exposure, basically acting as an annealing process, and resulting in crystal growth of the 100 oriented crystals. Further studies need to be conducted to confirm this result.

## 5. Outlook

In the next phase of the project, we propose the construction of an integrated "in-situ" characterization system to further develop the protocol for plasma-material exposure research. The proposed system consists of an Auger electron spectroscopy (AES) setup coupled with sputter depth profiling, temperature-programmed desorption spectroscopy (TPDS), and plasma-induced thermo-calorimetry (PTC) by accommodating "in-situ" sample transfer from the plasma exposure test bench, as shown in Fig. 6. Here, the central section (labeled "B") is the main target chamber; it is directly connected to the FRC plasma chamber using a 2-3/4" Con-Flat ceramic break and bellows assembly so as to ensure it is electrically isolated from the FRC system. A translating arm holds the sample so that its location from the end of the FRC position can be adjusted to vary the deposited energy density on the surface of the target. A region near the left of the target chamber contains a window for optical obser-vations of the target during impact. Fast framing cameras and spectrometers available at our laboratories would be used at this location. After the target is subjected to a sufficient number of FRC pulses, the translation arm associated with the chamber will be employed to retrieve the sample and move it into the main target analysis chamber. This is the heart of the "in-situ" analysis system that will be constructed during the early part of the next phase.

Auger electron spectroscopy (AES) will be used as a standard technique to characterize the surface compositions after plasma exposure. Compositional variations near the surface can be observed by $Ar^+$ ion depth profiling. A budget to install the AES hardware and software is included in this proposal. For selected samples, we will further use X-ray photoelectron spectroscopy (XPS) for chemical analysis, and the samples will be transferred using the mobile vacuum sample transfer device.

The retention of plasma fuel gases in the material will be characterized by temperature-programmable desorption spectroscopy (TPDS). In this method, a plasma-exposed sample is linearly heated, and the resulting flux of molecular species released is measured by a quadrupole mass spectrometer (QMS). From the release of molecular species, thermo-kinetic parameters related to molecular retention in the material will be determined.

The heat load imparted by the plasma will be directly characterized using calorimetric measurements. We will design and build a plasma-induced thermo-calorimetry (PTC) system to obtain heat deposition profile information from the impact of the FRC plasma on the target. Basically, this device consists of an array of graphite disks embedded on a circular copper supporting structure. The back of the graphite block contains a thermocouple to measure the increase in its temperature after being impacted by the FRC plasma. This 2-D array of graphite blocks will provide information on the energy deposition profile. Such data will in turn be used to characterize the FRC energy density and energy deposition profile. An infrared camera focused on the calorimeter may also be employed to obtain a second temperature measurement.

## 6. Conclusion

A small scale FRC plasma source was created for the purpose of conducting high density plasma-material interactions studies. The source is well characterized with a robust design and highly repeatable conditions over multiple shots. Plasma densities are on the order of 5 x $10^{21}$ $m^{-3}$, average ion velocities of approximately 300km/s, and kinetic energies ranging from $10kJ/m^2$ to $1MJ/m^2$. XPS depth profiling analysis revealed a Gaussian plasma jet structure approximately 1.2 cm in diameter propagating axially through the guide coils. Preliminary materials studies where performed for a variety of metals and ceramics. This serves to both provide direction in the next phase of the study and show the research group has both the tools and knowledge to perform these tasks. The Macor study revealed a thickness of roughly 2 mm for the sputter sheath of a Macor target at deuterium energy fluencies of $\sim 10kJ/m^2$, as well as differences in re-depostion thicknesses and densities depending on how the pellet was oriented relative to the surface. The beryllium oxide study showed clear evidence that sputtering rates and material damage depend on crystal orientation and showed some evidence that beryllium crystals oriented in the 100 direction on the surface might even be growing. Future plans to further equip the facility include the addition of an Auger spectrometer for in-situ chemical and depth profiling analysis, thermal desorption spectrometer to measure fuel gas desorption rates and a plasma induced thermo-calorimetry detector directed at the sample surface during exposures. These future characterization tools will further enhance the overall design of the plasma-materials research test bed and provide a unique opportunity to study the many effects of high energy high fluence plasma exposures on solid state materials.

# References

[1] M.G. Kong, B. N. Ganguly and R. F. Hicks: *Plasma Jets and Plasma Bullets*, ***Plasma Sources Sci. and Tech,*** (21), 3, (2012)

[2] D.A. Gurnett, A. Bhattacharjee: *Introduction to Plasma Physics: With Space and Laboratory Applications*. Cambridge, UK: Cambridge University Press. (2005)

[3] T Weber, J. Slough, D. Kirtley, *Rev. Sci. Instrum*. **83**, 113509 (2012).

[4] M. Tuszewski, *Nuclear Fusion* ***28,*** 2033 (1988).

[5] A. L. *Hoffman: Field Reversed Configuration and Rotating Magnetic Field Current Drive*, ***Course Notes***, University of Washington Department of Aeronautics & Astronautics. (2006)

[6] M. Kitajima: *Defects in Crystals Studied by Raman Scattering*, ***Solid State and Mat. Sci.,*** (22), 4. (1997)

[7] I.H. Hutchinson, Principles of Plasma Diagnostics. Cambridge: Cambridge University Press, 1987.

[8] S. Messer, A. Case, R. Bomgardner, M. Phillips, and F.D. Witherspoon, *Physics of Plasmas* ***16****, 064502 (2009)*

[9] MACOR® is a commercially produced by Corning, NY. Specific information about the product can be found at: http://www.corning.com/specialtymaterials/products_capabilites/macor.aspx

[10] J. W. McCauley, R. E. Newnham, G. V. Gibbs, ‘Crystal Structure Analysis of Synthetic Fluorophlogopite’, *American Mineralogist*, Volume 58, pages 249-254, 1973

[11] V. Barabash, R. Eaton, T. Hirai, I. Kupriyanov, G. Nikolaev, Z. Wang, X. Liu, M. Roedig, J. Linke: *Summary of beryllium qualification activity for ITER first-wall applications*, Phys. Scr. **T145** (2011) 014007